Features of microstructure and thermoelectric properties of the cermet composites based on grained Bi_2Te_3 matrix with locally-gradient $Ni@NiTe_2$ inclusions

Oleg Ivanov [a,*], Maxim Yaprintsev [b], Alexei Vasil'ev [a], Marina Zhezhu [b], Vseslav Novikov [a,b]

[a] Belgorod State Technological University named after V.G. Shukhov, Belgorod 308012, Russia
[b] Belgorod State University, Belgorod 308015, Russia

ARTICLE INFO

ABSTRACT

Starting Bi_2Te_3 and Ni powders were spark-plasma-sintered (SPS) to prepare thermoelectric cermet composites consisting of thermoelectric Bi_2Te_3 matrix with different content, x, of ferromagnetic Ni filler ($x = 0.00$, 0.50, 0.85, 1.25 and 1.50 at. %). Grained Bi_2Te_3 matrix of composites is texturing under sintering. Texturing degree is x-dependent that is attributed to ability of Ni particles act as lubricant. New trigonal $NiTe_2$ phase is formed under SPS-process. The Ni and $NiTe_2$ phases correspond to filler $Ni@NiTe_2$ ("core"-"shell") inclusions. Forming these inclusions is originated from chemical interaction between Bi_2Te_3 and Ni during SPS-process. A $Ni \rightarrow NiTe_2$ reaction is accelerated with increasing x that results in growing $Ni@NiTe_2$ inclusions and increasing fraction of shell. Thermoelectric properties of composites are x-dependent that is due to non-monotonic changes in texturing degree, size of the inclusions and concentration of majority carriers with increasing x. Thermoelectric figure-of-merit of composites is remarkably enhancing as compared to that of Bi_2Te_3 matrix.

1. Introduction

One of promising approaches of modern thermoelectric materials science, which can result in remarkable enhancing thermoelectric efficiency of materials, is developing micro (nano) composites, which are based on a matrix of thermoelectric material with filler magnetic inclusions, randomly distributed inside the matrix [1–3]. In this case, several physical mechanisms are simultaneously involved, which can affect the thermoelectric properties of these composites, including the specific electrical resistivity, ρ, the Seebeck coefficient, S, and the total thermal conductivity, k. The main mechanisms can be listed as follows [1–8]: (a) acting of the inclusions as scattering centres for electrons and phonons that affect ρ and k, respectively; (b) implementing of electron energy filtration effect, related to matrix/filler interfaces, that increases S; (c) involving of magnetic moments of the inclusions in scattering of electrons (similarly to the Kondo effect) that decreases electron mobility; (d) forming rectifying metal-semiconductor contact, related to matrix/filler interface, that increases electron concentration; (e) localization of electrons near matrix/filler interface that decreases the electron mobility; (f) paramagnon drag due to entrainment of electrons by paramagnons that affects ρ, S and k. Optimal tuning of ρ, S and k can maximize the thermoelectric figure-of-merit, $ZT=TS^2/\rho k$ (T is the absolute temperature) of material, which is applied as

matrix in composite [9]. Generally, the matrix of thermoelectric composite with the magnetic inclusions is grained semiconducting material, whereas the filler magnetic inclusions are transient *d*- or *f*-metals or alloys, based on these metals. Thus, these thermoelectric composites should be considered as cermet composites. Usually, the cermet composites serve as structural materials, which possess high temperature resistance and hardness, ability to undergo plastic deformation, etc. [10–12]. In contrast to the structural cermet composites, the thermoelectric cermet composites with the metallic magnetic inclusions are functional materials, since embedding the inclusions into the matrix should primarily improve the specific thermoelectric (functional) properties of the composite. At present, the composite, consisting of the grained Bi_2Te_3 matrix with the metallic Ni filler, can be considered as one of promising thermoelectric cermet composites with magnetic inclusions [13,14]. Matrix Bi_2Te_3 semiconductor is usually applied as end member to prepare *n*-type $Bi_2Te_{3-x}Se_x$ and *p*-type $Bi_{2-x}Sb_xTe_3$ alloys for various low-temperature thermoelectric applications [15,16]. Ni filler itself is known to be ferromagnet with the Curie temperature at 628 K [17]. The aim of present work is to find and analyze in detail features in the microstructure and thermoelectric properties of the Bi_2Te_3+xNi composites with different filler content, *x*.

2. Materials and methods

Mixtures of starting Bi_2Te_3 and Ni powders were used to prepare the composites with different Ni content (*x* = 0.00, 0.50, 0.85, 1.25 and 1.50 at. %). The starting Bi_2Te_3 powder was synthesized by "soft" chemistry methods. High-pure Bi_2O_3 and TeO_2 precursors were taken in stoichiometric ratio and dissolved in ethylene glycol. Alkaline agent (KOH) was also added to control pH-value. This solution was transferred in a round-bottom flask, which was then heated to boiling point. The boiling resulted in evaporation of water impurity. Just after evaporation, the flask sealed with reflux and maintained at 458 K for 4 h. The chemical synthesis resulted in formation of a dark suspension, which was cooled to room temperature. This suspension was purified by filtration and washing for 3 times with ethanol and acetone. Finally, synthesized powder was dried in argon atmosphere at 523 K for 2 h. To prepare the Ni powder, 5 g $Ni(NO_3)\bullet6H_2O$ was dissolved in 400 ml ethylene glycol. Then, 10 g KOH was added into this solution. The obtained mixture was heated to 353 K under vigorously stirring in order to form homogeneous sol. The sol was then cooled to room temperature. After, hydrazine hydrate was slowly added into the sol. This reaction mixture was heated to 373 K and maintained to 1 h in order to complete a reduction $Ni^{2+}{\rightarrow}Ni^0$ process. The Ni powder was extracted by a neodymium magnet and washed with ethanol and acetone in order to remove organic impurities. The starting Bi_2Te_3 and Ni powders were taken in ratio, corresponding to definite *x*, and mixed by a planetary mill for 30 min. These mixtures of the starting powders were spark plasma sintered (SPS) at pressure of 40 MPa and temperature of 573 K for 2 min. After SPS-process, Ø20 × 15 mm cylinders were obtained. To study the thermoelectric properties of the bulk samples, 2 × 2 × 10 mm bars and Ø10 × 2 mm disks were prepared.

The Archimedes' method was applied to measure density of the bulk samples. A model JEM - 2100 transmission electron microscope (TEM) was involved to examine morphology of the starting powders and estimate average size of particles in the powders. X-ray diffraction (XRD) analysis, performed by using a Rigaku Ultima IV diffractometer with CuK_{α}-radiation, was applied to study phase composition of the starting powders and the bulk samples. Scanning electron microscopy (SEM, a Nova NanoSEM 450 microscope) was applied to examine grain structure of the bulk samples, distinguish different phases, related to the filler inclusions (by backscattered electron (BSE) method), and take profiles of elements along line, crossing the inclusions (by energy dispersive X-ray spectroscopy (EDS) method). Bar samples were applied to measure the specific electrical resistivity and the Seebeck coefficient of the composites by using a ZEM-3 system. Disk-shaped samples were applied to measure the total thermal conductivity of the composites by using a TC-1200 system (a laser flash method). Using the Hall effect examination, performed by a Mini Cryogen Free Measurements System (Cryogenic Ltd, UK), concentration of electrons *n*, in the composites, was estimated.
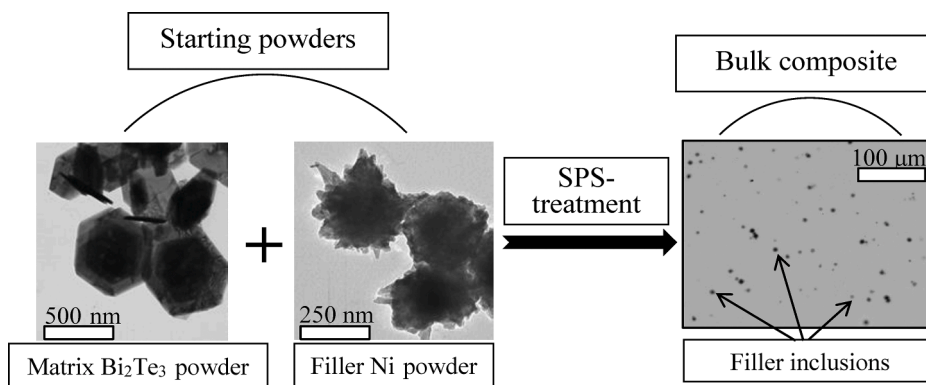

Fig. 1. Forming the matrix-filler microstructure of the bulk cermet composite with *x* = 0.5 at. % (BSE-image) under SPS-process of the relevant starting Bi_2Te_3 (TEM-image) and Ni (SEM-image) powders.

3. Results and discussion

3.1. Forming the bulk cermet Bi_2Te_3+xNi composites under SPS-treatment of the starting Bi_2Te_3 and Ni powders

Before analyzing features of the microstructure and thermoelectric properties of the cermet Bi_2Te_3+xNi composites, main patterns of their formation should be considered in brief [13,14]. The starting single-phased Bi_2Te_3 powder (hexagonal $R\overline{3}m$ structure with lattice $a = 0.4354$ nm and $c = 3.035$ nm parameters), which mainly consisted of hexagonal plates with average plate size of several hundreds of nm and width of ~100 nm, was applied to get grained matrix of the composite. Under chemical synthesis of Bi_2Te_3-based compounds, hexagonal 2D-plates are usually forming. Shape of particles in the starting Bi_2Te_3 powder is related to specific features of crystal layered structure and chemical mixed between covalent and Van-der-Waals bonds, which are specific for Bi_2Te_3-based materials [15,16,18]. The starting single-phased Ni powder (cubic face-centered $Fm\overline{3}m$ phase with $a = 0.3525$ nm), was applied as the filler in the composite. Particles of this powder are agglomerating in formations, which are almost spherical shape with diameter of 250–300 nm. Agglomerating Ni particles can be attributed to ferromagnetic interaction between the particles. Size of separate Ni particles is equal to several dozens of nm. Forming the matrix-filler microstructure of the composite with $x = 0.5$ at. % is schematically shown in Fig. 1. Under SPS-process, the starting Bi_2Te_3 (TEM-image, left part) and Ni (SEM-image, left part) powders are really transforming into the matrix-filler microstructure (right part, BSE-image). The filler inclusions, which are shown as separate darker islands, are randomly distributed inside the homogeneous gray matrix.

During SPS-treatment of the starting Bi_2Te_3 and Ni powders, a change of the phase composition was also found. XRD patterns for the composite with $x = 1.25$ at. %, which correspond to both the starting powders and the composite, are shown in Fig. 2. Besides expected Bi_2Te_3 and Ni phases, which are related to the relevant starting powders, a new $NiTe_2$ phase is observed in XRD pattern of the composite. The new phase is trigonal $P\overline{3}m1$ one with lattice $a = 0.3895$ and $c = 0.5470$ nm parameters. The most of peaks, which correspond to the Bi_2Te_3 and Ni phases, and the Bi_2Te_3 and $NiTe_2$ phases, are partially or totally overlapped in the XRD pattern of the composite. However, some of separate peaks for the Ni and $NiTe_2$ phases can be yet observed. The separate peaks are indicated by triangles for the Ni phase and circles for the $NiTe_2$ phase in upper-right XRD pattern. Therefore, XRD pattern for the composite is not simple superposition of relevant XRD patterns, corresponding to the starting Bi_2Te_3 and Ni powders. Enlarged parts of XRD pattern for the composite, showing the Ni phase and the $NiTe_2$ phase, are presented in inset to upper-right XRD pattern (for the Ni phase) and in
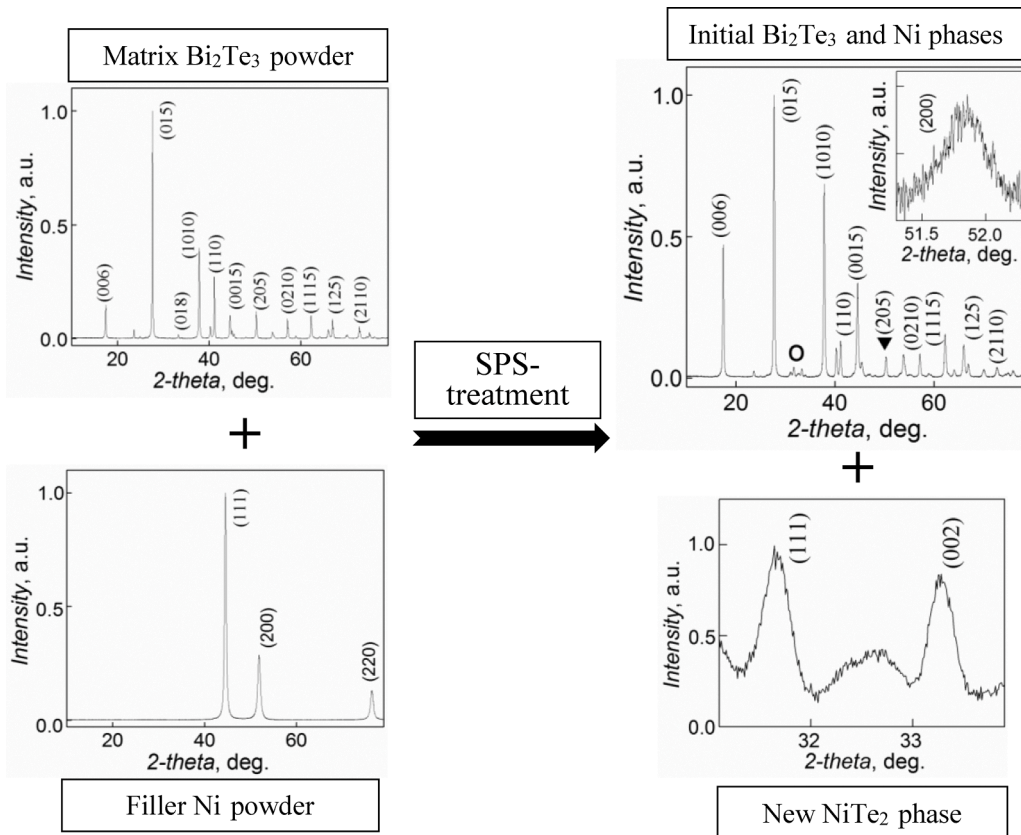

Fig. 2. Changing the phase composition of the composite with $x = 1.25$ at. % (left XRD patterns) under SPS-treatment of the relevant starting Bi_2Te_3 and Ni (c) powders (right XRD patterns).

separate lower-right XRD pattern (for the $NiTe_2$ phase).

The Ni and new $NiTe_2$ phases correspond to the filler inclusions. The filler inclusions are slightly distorted spherical "Ni core"-"$NiTe_2$ shell" ($Ni@NiTe_2$) inclusions. These inclusions were before named as locally-gradient domains [13,14]. BSE-image of one of the inclusions is shown in Fig. 3 (a). Results of EDS scanning, carried out along line, crossing this inclusion, are presented in Fig. 3 (b). One can see that (i) the shell dominantly consists of Ni and Te, (ii) the core dominantly contains Ni, (iii) far from the inclusion, Ni missis, whereas Te and Bi are homogenously distributed.

Thus, under SPS-treatment of the starting Bi_2Te_3 and Ni powders, the $Ni@NiTe_2$ inclusions are formed inside the Bi_2Te_3 matrix. During this $Ni{\rightarrow}NiTe_2$ transformation, the initial Ni inclusions act as impurity Ni sources. Initial Ni distribution within the matrix is strongly inhomogeneous. Under SPS-process, the matrix and filler atoms start diffusing through matrix/filler interfaces with trend to form homogeneous Ni distribution. Due to diffusion atoms redistribution the $Ni{\rightarrow}NiTe_2$ reaction is gradually implementing, resulting in forming the $NiTe_2$ shell, surrounding the Ni core.

3.2. Features of the microstructure of the bulk cermet Bi_2Te_3+xNi composites

Density of all the cermet Bi_2Te_3+xNi composites was weakly x-dependent and equal to $\sim$7.3 g·cm^{-3}, that is $\sim$95 % of theoretical value of the Bi_2Te_3 density (7.7 g/cm^3). To characterize the microstructure of the composites, features of the grained Bi_2Te_3 matrix and the filler $Ni@NiTe_2$ inclusions should be analyzed separately.

The main characteristics of the matrix are (i) an average grain size and (ii) a degree of preferential grain ordering. All the composites with different x are texturing under SPS-process. This texturing is typical for Bi_2Te_3-based compounds, which are prepared via uniaxial pressuring a starting powder [19–22]. A texturing axis is oriented along SPS-pressing direction. Under the texturing, the Bi_2Te_3 grains are preferentially orienting, resulting in forming a specific lamellar grain structure. Lamellar sheets are perpendicularly to SPS-pressing direction. Crystal c-axes of the separate grains are preferentially directed parallel to SPS-pressing direction, while crystal (a-b)-planes of the same grains are preferentially oriented perpendicularly to this direction. These features of the grain arrangement are shown in SEM-images for the composite with $x = 1.25$ at. %, taken from fractured surfaces, which are oriented perpendicularly or parallel to SPS-pressing direction (Fig. 4 (a) and (b), respectively). The elongated grains, forming the lamellar
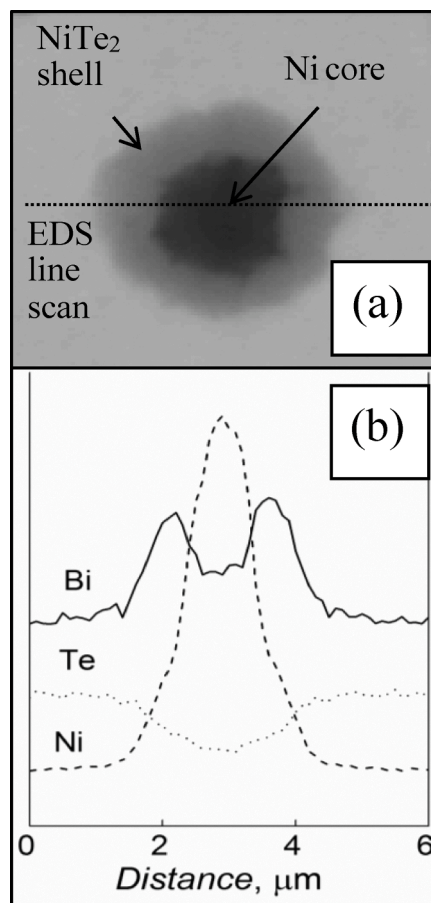

Fig. 3. BSE-image of the filler $Ni@NiTe_2$ inclusion (a) and EDS line scan profiles of Te, Bi and Ni, taken along line crossing the inclusion (b).
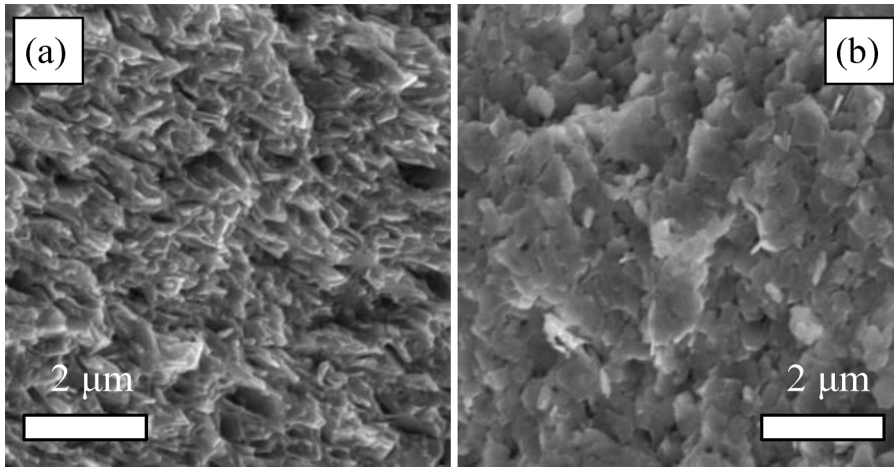
Fig. 4. SEM-images for the composite with $x = 1.25$ at. %, taken for the surfaces oriented parallel (a) and perpendicular (b) to SPS-pressing direction.

sheets, are clearly observed at the parallel surface. The grains, having mainly irregular shape, are observed at the perpendicular surface. Average grain sizes for directions, which are parallel ($D_\parallel$) and perpendicular ($D\perp$) to the SPS-pressing direction, are rather different. To estimate $D_\parallel$ and $D\perp$, histograms of grain size distribution were plotted and analyzed. The histograms were found to be obeyed a lognormal unimodal distribution [23]. The texturing degree was estimated via analysis of XRD patterns. This analysis allowed extracting the Lotgering factor, *LF* [24]. The *LF(x)*, *D⊥(x)* and $D_\parallel(x)$ dependences are shown in Fig. 5.

Filler free compound, i.e. the Bi_2Te_3 matrix itself, is least textured. Under gradual embedding the Ni filler into the matrix, *LF* is steady increasing with increasing x up to $x = 1.25$ at. %. But, for the composite with $x = 1.5$ at. %, *LF* is remarkably decreasing. This extreme *LF(x)* dependence can be attributed to competing two mechanisms, affecting *LF* in the opposite manner. With increasing the filler content, $D\perp$ demonstrates a general trend of weak growth with appearance of local minimum at $x = 0.5$ at. %, whereas $D_\parallel$ is x-independent. To characterize a grain shape factor, $D\perp/D_\parallel$ ratio was introduced. This ratio changes from minimal $\sim$4.2 value for $x = 0.5$ at. % to maximal $\sim$6.0 value for $x = 1.5$ at. %. The mechanisms, governing the *LF(x)*, *D⊥(x)* and $D_\parallel(x)$ behaviors, will be discussed below.

The main characteristics of the $Ni@NiTe_2$ inclusions are (i) an average inclusion size and (ii) an internal structure of the inclusion, which is characterized by a ratio between fractions of the core and the shell. Changing the filler inclusions in the composites with increasing x is shown in Fig. 6. By comparing BSE-images, taken for polished surfaces of the composites with $x = 0.5$, 0.85 and 1.5 at. % (top panel), one can conclude that a surface density of the inclusions (a number of the inclusions per unit of the surface) is expectedly
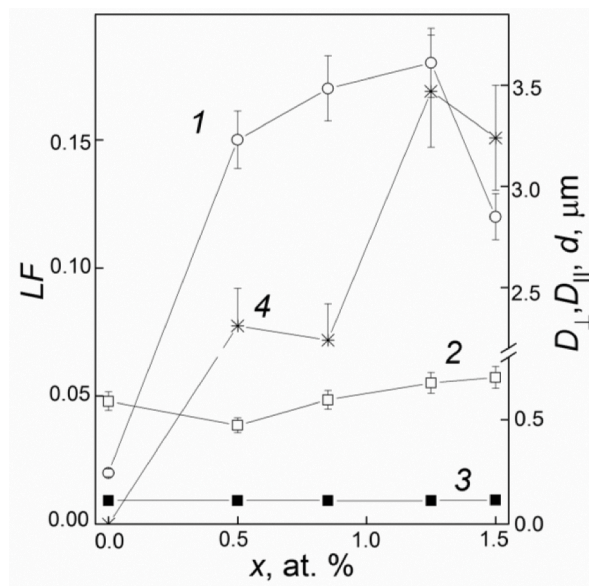

Fig. 5. The *LF* (curve *1*), *D⊥* (*2*), $D_\parallel$ (*3*) and *d* (*4*) vs. x dependences for the composites.
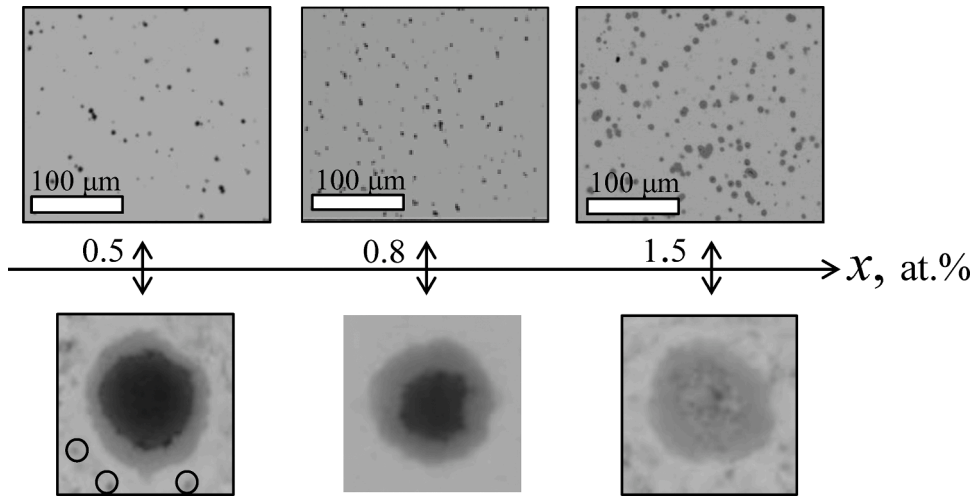
Fig. 6. Changing the filler Ni@NiTe$_2$ inclusions in the composites with increasing x. Top panel: BSE-images of surfaces for the composites with different x; bottom panel: typical BSE-images of the first, second and third type's inclusions.

increasing with increasing x. In contrast to ordering the grains under the texturing, no similar ordering can be found for the inclusions. Size of all the inclusions, d, corresponds to micro-sized range. A ratio between thickness of the shell, l, and radius of the core, r, is dependent on initial size of the Ni inclusions, which are gradually transforming into the "core"-"shell" inclusions under SPS-process. All the Ni@NiTe$_2$ inclusions can be roughly separated by three main types. The first type inclusions consist of the big core, but the thin shell, i.e. $d >$ (or $>>$) l. For the second type inclusions, d and l are approximately equal to each other. In the third type inclusions, the shell is dominated, i.e. $l >$ (or $>>$) d. Typical BSE-images for the first, second and third type's inclusions are shown in bottom panel of Fig. 6.

With increasing x, a fraction of the inclusions with dominant shell is visually increasing. In other words, for the composites with small filler content, the first type inclusions are dominant, whereas the third type inclusions are dominated for the composites with large filler content. The second type inclusions are characteristic for the composites with intermediate filler content.

To estimate d, histograms of inclusion size distribution were plotted and analyzed in frames of the lognormal unimodal distribution. The $d(x)$ dependence is added to Fig. 5. In general, this dependence is growing with increasing x. Thus, features in the filler system, which are characterized by size (d) and structure (l/d) of the Ni@NiTe$_2$ inclusions, are rather sensitive to the filler content. This sensitivity can be probably related to physical mechanisms, which act during SPS-process under uniaxial pressuring and pulse electrical current. A combination of electrical, mechanical and thermal factors is simultaneously involved in this case [25–27]. The sintering is initiated by periodically generated pulses of electric current. Under the pulse, energy is released on the powder particles during a pulse term. These particles are already under a constant set pressure. The compressed particles are heated by the Joule heating at contact points via repeated spark discharges. The discharges act between the gaps between the particles that results in faster thermal diffusion of atoms. Besides, the electrical discharges generate plasma, which escalates the sintering, too, via plasma ion-atoms interaction. The specific electrical resistivity of Ni and Bi$_2$Te$_3$ is different from each other. At room temperature, the Ni resistivity is equal to $\sim 6.5 \bullet 10^{-2}$ μΩ$\bullet$m [28], whereas the resistivity of textured Bi$_2$Te$_3$ samples, which were measured in this work, is equal to ~ 23 or ~ 30 μΩ$\bullet$m, dependent on measuring orientation (Fig. 7 (a) and (d)). Therefore, embedding the metallic Ni filler into the semiconductor Bi$_2$Te$_3$ matrix will result in strong electrical inhomogeneity of relevant cermet composite. The electrically inhomogeneous semiconductors are characterized by some spatial distribution of the inhomogeneities that results in continuously varying conductivity fluctuations [29–31]. In turn, this electrical inhomogeneity will redistribute the electrical current, resulting in macroscopically distorted current paths. Due to the lower Ni resistivity, the current will preferentially flow through the Ni inclusions. At increasing in x, relevant growing fraction of the current pulse, flowing through the inclusions, will take place. Therefore, the Ni→NiTe$_2$ reaction will be accelerated with the increasing in the Ni content that results in, firstly, growing the Ni@NiTe$_2$ inclusions, and, secondly, increasing fraction of the shell in these inclusions. Both these features can be confirmed by the experiments as is shown in Fig. 5 (curve 4) and bottom panel of Fig. 6.

Besides the micrometer filler Ni@NiTe$_2$ inclusions, other nanometer inclusions with size of <100 nm are also observed. As an example, these inclusions are highlighted by the rounds for the first type inclusions (bottom panel of Fig. 6). By comparing color of the nanometer inclusions and the NiTe$_2$ shell in the "core"-"shell" inclusions, one can conclude that the nanometer inclusions correspond to the NiTe$_2$ phase. As was mentioned above, the starting Ni powder consists of agglomerated formations, which include many Ni particles (Fig. 1). Due to chemical interaction between the Bi$_2$Te$_3$ matrix and the Ni filler, the nanometer NiTe$_2$ inclusions can be synthesized from these initial separate Ni particles, which, in turn, are formed under mixing the starting Bi$_2$Te$_3$ and Ni powders by the planetary mill. Since the separate Ni particles are small, they have a time enough to completely transform into the NiTe$_2$ phase inclusions under SPS-process. These separate Ni particles can act as a lubricant during spark plasma sintering of the cermet Bi$_2$Te$_3$+xNi composites. It is known [32] that the initial stage of SPS-process is a packing of the particles in the starting powder under external
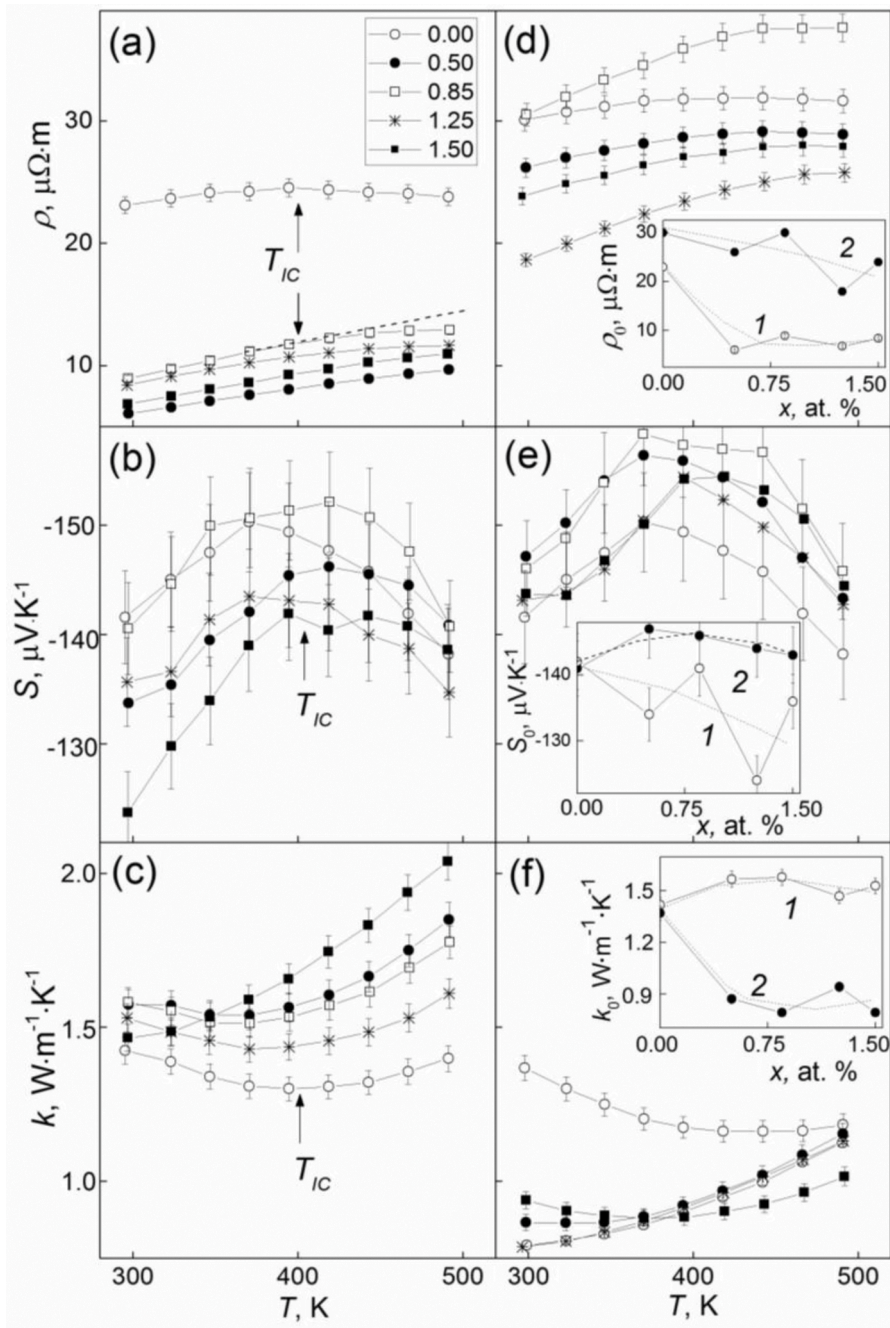
Fig. 7. Temperature dependences of ρ ((a) and (d)), S ((b) and (e)), and k ((c) and (f)) for the composites with different filler content, taken for the perpendicular (left panel) and parallel (right panel) measuring orientations. Insets to Figs. (d), (e) and (f) are the $\rho_0(x)$, $S_0(x)$ and $k_0(x)$ dependences, respectively, corresponding to the perpendicular (curves *1*) and parallel (*2*) measuring orientations.

pressuring. During the texturing, the packing results in the rearrangement of the randomly oriented particles into the lamellar sheets with preferential particles orientation. It is known that some nanometer powder lubricants improve the particles packing behavior during SPS-process. This lubricant effect was earlier reported for the Ce lubricant in Al_2O_3 [33] or the Te lubricant in Bi_2Te_3 [34]. In accordance with lubricating mechanism, increasing the Ni content will result in more effective packing the particles, and relevant increasing in preferential grain orientation in the Bi_2Te_3+xNi composites. As result, the Lotgering factor will be gradually growing. However, increasing the Ni content will be accompanied by the Ni→$NiTe_2$ transformation, and $NiTe_2$ is chemical compound. This compound cannot already act as lubricant. So, a lubricant efficiency of the initial Ni particles will be gradually reducing with increasing x that will negatively affect the particles packing and the following texturing. Competition of these two factors, acting in the

opposite manner, will form the extreme $LF(x)$ dependence (curve *1* in Fig. 5).

The Ni→NiTe$_2$ transformation can be also responsible for the weak $D\perp(x)$ growth with increasing x (curve *2* in Fig. 5). The initial nanometer Ni inclusions can act as some obstacles, blocking any movement of the grain boundary and, hence, preventing the grains growth [35]. However, the formed NiTe$_2$ phase is already located in the grain itself and it unable act as the obstacles during the grains growth. As result, the grain size will be increasing with increasing Ni content.

It should be also noted that preparation of the initial "core"-"shell" particles of various types is already known way, applying to improve the thermoelectric properties of materials [36,37]. However, at sintering a bulk material, the initial "core"-"shell" structure is usually destroyed [36]. In the cermet Bi$_2$Te$_3$+xNi composites, the Ni@NiTe$_2$ inclusions are naturally formed inside the bulk thermoelectric matrix during SPS-process. Moreover, size of the inclusions themselves, along with thickness of the shells and radius of the cores, can be believed to be tuned in desired manner via correct choosing the content and size of the initial Ni particles, and temperature and holding time of SPS-process.

Finally, NiTe$_2$, which is shell's material, is compound interesting for research. Particularly, at present this compound is considering as topological insulator [38,39]. Usually, NiTe$_2$ is prepared by direct alloying of Ni and Te. But, at preparation of the cermet Bi$_2$Te$_3$+xNi composites, the NiTe$_2$ phase is formed via the high-temperature diffusion redistribution of atoms and the chemical interaction between the Bi$_2$Te$_3$ matrix and filler Ni particles.

3.3. Features of the thermoelectric properties of the cermet Bi$_2$Te$_3$+xNi composites

All the thermoelectric properties, including the specific electrical resistance, the Seebeck coefficient and the total thermal conductivity of the cermet composites being studied, are dependent on the filler content. Besides, since the composites are textured, these properties are also anisotropic. To explore the texturing effect, the thermoelectric properties were measured for directions, which are perpendicular (perpendicular measuring orientation) and parallel (parallel measuring orientation) to SPS-pressing direction. The temperature dependences of ρ, S and k, taken for the cermet composites with different x for the perpendicular (left panel) and parallel (right panel) measuring orientations, are shown in Fig. 7. The main features in these dependences can be listed as follows.

Firstly, at the same filler content, the $\rho(T)$ curves for the perpendicular measuring orientation lie lower than the relevant $\rho(T)$ curves for the parallel measuring orientation, and the $k(T)$ curves for the perpendicular measuring orientation lie higher than the relevant $k(T)$ curves for the parallel measuring orientation. The texturing just results in redistributing the anisotropic ρ and k contributions from crystal *a-b* plane (ρ_{ab} and k_{ab}) and *c*-axis (ρ_c and k_c) into the specific electrical resistivity and the total thermal conductivity, measured
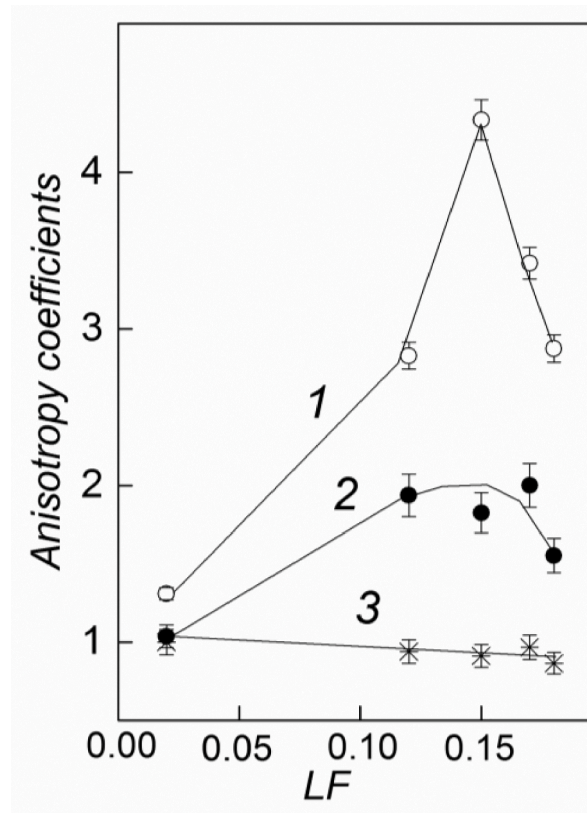

Fig. 8. *LF*-dependences of anisotropy coefficients $\rho_{\parallel}/\rho_{\perp}$ (curve *1*) $k_{t\perp}/kt_{\parallel}$ (*2*) and $S_{\parallel}/S_{\perp}$ (*3*) for the composites.

parallel (ρ_c and k_c are dominant contributions) or perpendicularly (ρ_{ab} and k_{ab} are dominant contributions) to the texturing axis [20]. Since $\rho_{ab} < \rho_c$ and $k_{ab} > k_c$, the electrical resistivity increases and the thermal conductivity decreases for the parallel measuring orientation as compared to these properties for the perpendicular measuring orientation. Secondly, the Seebeck coefficient is known to be very weakly anisotropic quantity [20]. However, in the cermet $Bi_2Te_3 + x$Ni composites with the same filler content, the $S(T)$ curves for the parallel measuring orientation lie higher than relevant $S(T)$ curves for the parallel measuring orientation, i.e. S unexpectedly happened to be rather anisotropic. Reason of this S anisotropy is unclear now. Sign of the Seebeck coefficient is negative. So, majority carriers in the composites are electrons. Thirdly, the temperature behaviors of all the thermoelectric properties of the composites are typical for Bi_2Te_3 and Bi_2Te_3-based compounds [40–42]. Specific features in these dependences can be attributed to onset of intrinsic conductivity, which is related to thermal excitation of carriers from valence band to conduction band. Temperature T_{IC}, at which the intrinsic conductivity appears, is indicated by arrows in Fig. 7. For all the measuring orientations, the intrinsic conductivity is accompanied by appearance of kinks or maxima in the $\rho(T)$ dependences, maxima in the $S(T)$ dependences and minima in the $k(T)$ dependences. To not complicate Fig. 7, the arrows are shown only for the perpendicular measuring orientation. Detailed explanations of physical mechanisms, resulting in changing the thermoelectric properties at T_{IC}, can be found in Refs. [20,40–43]. Finally, the x-effect on the thermoelectric properties of the cermet $Bi_2Te_3 + x$Ni composites is rather complicated, since all the properties are non-monotonically changed with increasing x. The x-dependent thermoelectric properties, measured for the perpendicular (curves *1*) and parallel (*2*) measuring orientations at room temperature, ρ_0, S_0 and k_0, are shown in insets to Fig. 7 (b), (e) and (f), respectively. However, some general trends, shown by dashed curves in the insets, can be yet found in these non-monotonic dependences. The trends, which are helpful to enhance the thermoelectric figure-of-merit, are a decreasing the specific electrical resistivity (for both measuring orientations, inset to Fig. (d)), a weak growing the Seebeck coefficient (for the parallel measuring orientation, inset to Fig. (e)) and a decreasing the total thermal conductivity (for the parallel measuring orientation, inset to Fig. (f)). The non-monotonic behavior of the thermoelectric properties can be originated from simultaneous action of several mechanisms, which can affect the specific features of the composites with different x. Moreover, strength of each mechanism is x-dependent. The main mechanisms are as follows: (a) changing the preferential grain orientation (texturing degree), expressed by the Lotgering factor (curve *1* in Fig. 5); (b) changing the average size of the filler inclusions (curve *4* in Fig. 5); (c) forming the "core"-"shell" inclusions, and a fraction of the shell is increasing with increasing x (Fig. 6); (d) gradual changing the properties of the "core"-"shell" inclusions via relevant changing the shell/core ratio (in particularly, decreasing the size of the ferromagnetic Ni score should be accompanied by weakening the magnetic properties).

To take into account the texturing degree effect, the *LF*-dependences of anisotropy coefficients of the thermoelectric properties, $\rho_{II}/\rho\perp$, $k_t\perp/kt_{II}$, and $S_{II}/S\perp$ (where II and $\perp$ subscripts correspond to the parallel and perpendicular measuring orientations, respectively) were plotted (Fig. 8). Anisotropy in the Seebeck coefficient is least expressed (curve *3*), but clear maxima are observed in anisotropy coefficients of the specific electrical resistivity (*1*) and the total thermal conductivity (*2*). Appearing the maxima is rather unexpected, since increasing the texturing degree should result in relevant increasing anisotropy of the properties. This behaviour is observed for left side of the maxima. Therefore, only changing the texturing degree cannot be responsible for x-dependent changing the thermoelectric properties within whole x range.

Analysis of the inclusions size effect on the thermoelectric properties of the composites is complicated task, since although each of the size (d) corresponds to relevant x, but, in turn, *LF* is strongly x-dependent, too. However, it is important to note that at increasing x, d, ρ_0, S_0 and k_0 are mainly changed in qualitatively similar manner (curve *4* in Fig. 5 and curves in insets to Fig. 7). Therefore, d-effect on the thermoelectric properties can be believed to really take place. Usually, this effect is attributed to electron and phonon scattering by the inclusions [44,45].

The thermoelectric properties of the composites could be also varied due to x-dependent changing concentration of electrons (n). To estimate n, the Hall effect was examined. The $n(x)$ dependence is presented in Fig. 9. This dependence has a maximum at $x = 0.85$ at. %. It is obviously that a source of the electrons in the composites is metallic Ni. With increasing x, on the one hand, the Ni content in the initial filler inclusions increases, resulting in increasing n, but, on the other hand, a fraction of the Ni core in the inclusions decreases, resulting in decreasing n. A competition of these trends forms the relevant $n(x)$ maximum. In turn, with increasing x, the thermoelectric properties should be changed in the following manner: ρ and S are decreasing, whereas k is increasing (due to increasing in the electron thermal conductivity) [46,47].

Thus, the complicated x-effect on the thermoelectric properties of the cermet $Bi_2Te_3 + x$Ni composites is really due to involving several interacting mechanisms. Besides, one can conclude that to examine this x-effect correctly and in detail, the technological parameters of SPS-process should be thoroughly tuned for each of Ni contents used. This fine tuning will allow optimizing all the thermoelectric properties for all the compositions.

The $\rho(T)$, $S(T)$, and $k(T)$ dependences were applied to calculate and plot the temperature dependences of ZT (Fig. 10 (a) and (b)). These dependences are bell-shaped. Owing to better combination of ρ, S, and k, the thermoelectric figure-of-merit is remarkably higher for the perpendicular measuring orientation. Although the x-effect on ZT is also complicated, one can conclude that all the cermet $Bi_2Te_3 + x$Ni composites demonstrate enhanced thermoelectric efficiency as compared to that for the thermoelectric Bi_2Te_3 matrix.

The x-dependences of maximum ZT values, ZT_{max}, calculated for the perpendicular (curve *1*) and parallel (*2*) measuring orientations, are shown in inset to Fig. 10 (b). The highest $ZT_{max} \approx 0.67$ corresponds to the composite with $x = 0.5$ at % at the perpendicular measuring orientation. That is in accordance with preliminary results, more than two-fold enhancement of ZT (~0.67 for the composite against $ZT_{max} \approx 0.30$ for the thermoelectric Bi_2Te_3 matrix) can be yielded in the cermet $Bi_2Te_3 + x$Ni composites. As was mentioned in Introduction part, many physical mechanisms can be simultaneously affected the thermoelectric properties of the cermet composites with magnetic inclusions. To correctly find the physical mechanisms, responsible for observed changes of the thermoelectric properties of the cermet $Bi_2Te_3 + x$Ni composites, further experimental work should be carried out.
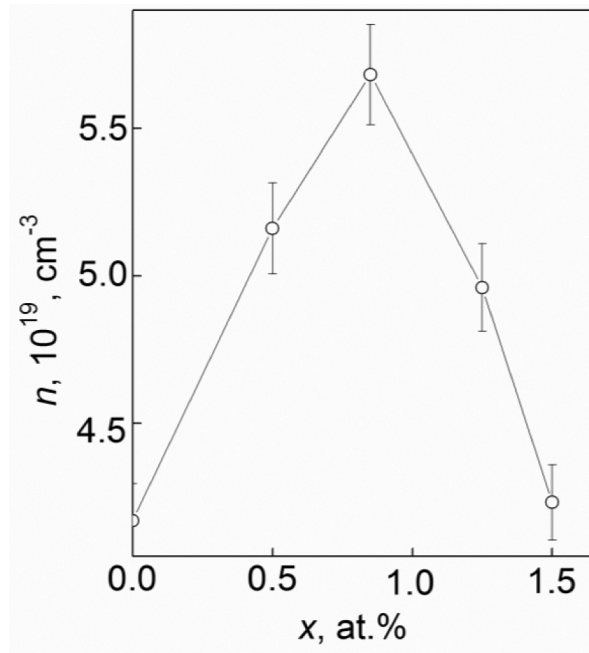
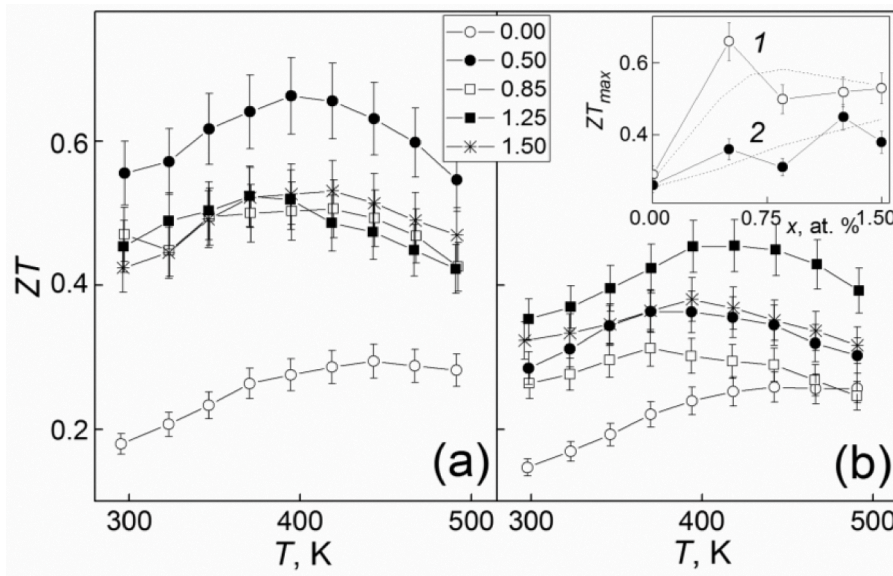**Fig. 9.** The $n(x)$ dependence for the composites.

Fig. 10. The temperature dependences of ZT for the composites with different filler content, taken for the perpendicular (a) and parallel (b) measuring orientations. Inset is the ZT_{max} vs. x dependences corresponding to the perpendicular (curve *1*) and parallel (*2*) measuring orientations.

4. Conclusion

Thus, features in the microstructure and thermoelectric properties of the thermoelectric cermet Bi_2Te_3+xNi composites with different filler Ni content, prepared by spark plasma sintering, have been found and analyzed. As was reported earlier, during SPS-treatment, the initial Ni inclusions in these composites are gradually transforming into the locally-gradient Ni@NiTe$_2$ inclusions [13,14]. Here we report, in which manner forming these Ni@NiTe$_2$ inclusions allows governing the thermoelectric properties of the thermoelectric Bi_2Te_3 matrix. The main mechanisms, affecting the thermoelectric properties, are related to features in the microstructure of the composites (texturing degree of the matrix, size and internal structure of the inclusions), and donor-like effect of the inclusions, resulting in non-monotonic x-dependent change of the electron concentration. Efficiency of these interacting mechanisms is

x-dependent.

Declaration of Competing Interest

The authors declare that they have no known competing financial interests or personal relationships that could have appeared to influence the work reported in this paper.

Acknowledgments

References

[1] W. Zhao, Z. Liu, P. Wei, Q. Zhang, W. Zhu, X. Su, X. Tang, J. Yang, Y. Liu, J. Shi, Y. Chao, S. Lin, Y. Pei, Magnetoelectric interaction and transport behaviours in magnetic nanocomposite thermoelectric materials, Nat. Nanotechnol. 12 (2017) 55–60, https://doi.org/10.1038/nnano.2016.182.

[2] W. Zhao, Z. Liu, Z. Sun, Q. Zhang, P. Wei, X. Mu, H. Zhou, C. Li, S. Ma, D. He, P. Ji, W. Zhu, X. Nie, X. Su, X. Tang, B. Shen, X. Dong, J. Yang, Y. Liu, J. Shi, Superparamagnetic enhancement of thermoelectric performance, Nature 13 (2017) 247–251, https://doi.org/10.1038/nature23667.

[3] R. Lu, J.S. Lopez, Y. Liu, T.P. Bailey, A.A. Page, S. Wang, C. Uher, P.F.P. Poudeu, Coherent magnetic nanoinclusions induce charge localization in half-Heusler alloys leading to high T_c ferromagnetism and enhanced thermoelectric performance, J. Mater. Chem. A 7 (2019) 1095–11103, https://doi.org/10.1039/c9ta01156k.

[4] A.J. Minnich, M.S. Dresselhaus, Z.F. Ren, G. Chen, Bulk nanostructured thermoelectric materials: current research and future prospects, Energy Environ. Sci. 2 (2009) 466–479, https://doi.org/10.1039/b822664b.

[5] C.J. Vineis, A. Shakouri, A. Majumdar, M.G. Kanatzidis, Nanostructured thermoelectrics: big efficiency gains from small features, Adv. Mater. 22 (2010) 3970–3980, https://doi.org/10.1002/adma.201000839.

[6] W. Liu, X. Yan, G. Chen, Z. Re, Recent advances in thermoelectric nanocomposites, Nano Energy 1 (2012) 42–56, https://doi.org/10.1016/j.nanoen.2011.10.001.

[7] J.H. Bahk, Z. Bian, A. Shakouri, Electron energy filtering by a nonplanar potential to enhance the thermoelectric power factor in bulk materials, Phys. Rev. B 87 (2013) 1–13, https://doi.org/10.1103/PhysRevB.87.075204.

[8] Z. Peng, D. He, X. Mu1, H. Zhou, C. Li, S. Ma, P. Ji, W. Hou, P. Wei, W. Zhu, X. Nie, W. Zhao, Preparation and enhanced thermoelectric performance of Cu2Se-SnSe composite materials, J. Electron. Mater. 47 (2018) 3350–3357, https://doi.org/10.1007/s11664-018-6218-5.

[9] G.J. Snyder, Figure of merit ZT of a thermoelectric device defined from materials properties, Energy Environ. Sci. 10 (2017) 2280–2283, https://doi.org/10.1039/c7ee02007d.

[10] D.M. Sun, X.S. Jiang, H.L. Sun, T.F. Song, Z.P. Luo, Microstructure and mechanical properties of Cu-ZTA cermet prepared by vacuum hot pressing sintering, Mater. Res. Express. 7 (2020) 1–13, https://doi.org/10.1088/2053-1591/ab6c19.

[11] Y. Zheng, Y. Zhou, R. Li, J. Wang, L. Chen, S. Li, Preparation and mechanical properties of TiC-Fe Cermets and TiC-Fe/Fe Bilayer Composites, J. Mater. Eng. Perform. 26 (2017) 4933–4939, https://doi.org/10.1007/s11665-017-2914-1.

[12] V. Verma, B.V. Manoj Kumar, Synthesis, microstructure and mechanical properties of Al2O3/ZrO2/CeO2 composites with addition of nickel and titania processed by conventional sintering, Mater. Today Proc. 4 (2017) 3062–3071, https://doi.org/10.1016/j.matpr.2017.02.189.

[13] M. Yaprintsev, A. Vasil'ev, O. Ivanov, M. Zhezhu, E. Yaprintseva, V. Novikov, Enhanced thermoelectric efficiency of the bulk composites consisting of "Bi2Te3 matrix" and "filler Ni@NiTe2 inclusions, Scr. Mater. 194 (2021) 1–4, https://doi.org/10.1016/j.scriptamat.2020.113710.

[14] M. Yaprintsev, A. Vasil'ev, O. Ivanov, M. Zhezhu, E. Yaprintseva, V. Novikov, Forming the locally-gradient Ni@NiTe2 domains from initial Ni inclusions embedded into thermoelectric Bi2Te3 matrix, Mater. Lett. 290 (2021) 1–4, https://doi.org/10.1016/j.matlet.2021.129451.

[15] H.J. Goldsmid, Bismuth telluride and its alloys as materials for thermoelectric generation, Mater 7 (2014) 2577–2592, https://doi.org/10.3390/ma7042577.

[16] H. Scherrer, S. Scherrer, Thermoelectrics Handbook: Macro to Nano, CRC Taylor and Francis, Boca Raton, 2012.

[17] B.D. Cullity, C.D. Graham, Introduction to Magnetic Materials, IEEE Press, Piscataway, 2009.

[18] J.R. Drabble, C.H.L. Goodman, Chemical bonding in bismuth telluride, J. Phys. Chem. Solids 5 (1958) 142–144, https://doi.org/10.1016/0022-3697(58)90139-2.

[19] S.D. Bhame, D. Pravarthana, W. Prellier, J.G. Noudem, Enhanced thermoelectric performance in spark plasma textured bulk *n*-type Bi2Te2.7Se0.3 and *p*-type Bi0.5Sb1.5Te3, Appl. Phys. Lett. 102 (2013) 1–3, https://doi.org/10.1063/1.4807771.

[20] O. Ivanov, M. Yaprintsev, A. Vasil'ev, Comparative analysis of the thermoelectric properties of the non-textured and textured Bi1.9Gd0.1Te3 compounds, J. Solid State Chem. 290 (2020) 1–10, https://doi.org/10.1016/j.jssc.2020.121559.

[21] Q. Lognon, F. Gascoin, O.I. Lebedev, L. Lutterotti, S. Gascoin, D. Chateigner, Quantitative texture analysis of spark plasma textured *n*-Bi2Te3, J. Am. Ceram. Soc. 97 (2014) 2038–2045, https://doi.org/10.1111/jace.12970.

[22] J.J. Shen, L.P. Hu, T.J. Zhu, X.B. Zhao, The texture related anisotropy of thermoelectric properties in bismuth telluride based polycrystalline alloys, Appl. Phys. Lett. 99 (2011) 1–3, https://doi.org/10.1063/1.3643051.

[23] F.J. Humphreys, M. Hatherly, Recrystallization and Related Annealing Phenomena, Elsevier, Oxford, UK, 2004.

[24] F.K. Lotgering, Topotactical reactions with ferrimagnetic oxides having hexagonal crystal structures-I, J. Inorg. Nucl. Chem. 9 (1959) 113–123, https://doi.org/10.1016/0022-1902(59)80070-1.

[25] R. Chaim, Densification mechanisms in spark plasma sintering of nanocrystalline ceramics, Mater. Sci. Eng. A 443 (2007) 25–35, https://doi.org/10.1016/j.msea.2006.07.092.

[26] D. Perera, M. Tokita, S. Moricca, Comparative study of fabrication of Si3N4/SiC composites by spark plasma sintering and hot isostatic pressing, J. Eur. Ceram. Soc. 18 (1998) 401–404, https://doi.org/10.1016/S0955-2219(97)00139-8.

[27] S.X. Song, Z. Wang, G.P. Shi, Heating mechanism of spark plasma sintering, Ceram. Int. 39 (2013) 1393–1396, https://doi.org/10.1016/j.ceramint.2012.07.080.

[28] T. Farrell, D. Greig, The electrical resistivity of nickel and its alloys, J. Phys. C Solid State Phys. 1 (1968) 1359–1369, https://doi.org/10.1088/0022-3719/1/5/326.

[29] R. Xu, A. Husmann, T.F. Rosenbaum, M.L. Saboungi, J.E. Enderby, P.B. Littlewood, Large magnetoresistance in non-magnetic silver chalcogenides, Nature 390 (1997) 57–60, https://doi.org/10.1038/36306.

[30] H.G. Johnson, S.P. Bennett, R. Barua, L.H Lewis, D. Heiman, Universal properties of linear magnetoresistance in strongly disordered MnAs-GaAs composite semiconductors, Phys. Rev. B 82 (2010) 1–4, https://doi.org/10.1103/PhysRevB.82.085202.

[31] J. Hu. M.M. Parish, T.F. Rosenbaum, Nonsaturating magnetoresistance of inhomogeneous conductors: comparison of experiment and simulation, Phys. Rev. B 75 (2007) 1–9, https://doi.org/10.1103/PhysRevB.75.214203.

[32] L. Wang, V. Pouchly, K. Maca, Z. Shen, Y. Xiong, Intensive particle rearrangement in the early stage of spark plasma sintering process, J. Asian Ceram. Soc. 3 (2015) 183–187, https://doi.org/10.1016/j.jascer.2015.02.004.

[33] I. Alvarez-Clemares, G. Mata-Osoro, A. Fernandez, S. Lopez-Esteban, C. Pecharroman, J. Palomares, R. Torrecillas, J. Serafin Moya, Transparent alumina/ceria nanocomposites by spark plasma sintering, Adv. Eng. Mater. 12 (2010) 1154–1160, https://doi.org/10.1002/adem.201000176.

[34] Y. Liu, Y. Zhang, K.H. Lim, M. Ibáñez, S. Ortega, M. Li, J. David, S. Martí-Sánchez, K.M. Ng, J. Arbiol, M.V. Kovalenko, D. Cadavid, A. Cabot, High thermoelectric performance in crystallographically textured *n*-type $Bi_2Te_{3-}x Se x$ produced from asymmetric colloidal nanocrystals, ACS Nano 12 (2018) 7174–7184, https://doi.org/10.1021/acsnano.8b03099.

[35] P. Boch, A. Leriche, P. Boch, J.C. Niepce, Sintering and microstructure of ceramics, ISTE Ltd, London, 2007, pp. 75–77. Ceramic Materials: Processes, Properties and Applications.

[36] O. Ivanov, O. Maradudina, R. Lyubushkin, Preparation and characterization of bulk composite constructed of $Bi_2Te_3@SiO_2$ nanoparticles, J. Alloy. Compd. 586 (2014) 679–682, https://doi.org/10.1016/J.JALLCOM.2013.10.090.

[37] J.H. Bahk, P. Santhanam, Z. Bian, R. Ram, A. Shakouri, Resonant carrier scattering by core-shell nanoparticles for thermoelectric power factor enhancement, Appl. Phys. Lett. 100 (2012) 1–4, https://doi.org/10.1063/1.3673615.

[38] Q. Liu, F. Fei, B. Chen, X. Bo, B. Wei, S. Zhang, M. Zhang, F. Xie, M. Naveed, X. Wan, F. Song, B. Wang, Nontopological origin of the planar Hall effect in the type-II Dirac semimetal $NiTe_2$, Phys. Rev. B 99 (2019) 1–7, https://doi.org/10.1103/PhysRevB.99.155119.

[39] J. Zhang, G.Q. Huang, The superconductivity and topological surface state of type-II Dirac semimetal $NiTe_2$, J. Phys. Condens. Matter. 32 (2020) 1–9, https://doi.org/10.1088/1361-648X/ab6f84.

[40] M. Yaprintsev, R. Lyubushkin, O. Soklakova, O. Ivanov, Effects of Lu and Tm doping on thermoelectric properties of Bi_2Te_3, J. Electron. Mater. 47 (2018) 1362–1370, https://doi.org/10.1007/s11664-017-5940-8.

[41] O. Ivanov, M. Yaprintsev, Mechanisms of thermoelectric efficiency enhancement in Lu-doped Bi_2Te_3, Mater. Res. Express 5 (2018) 1–10, https://doi.org/10.1088/2053-1591/aaa265.

[42] X.H. Ji, X.B. Zhao, Y.H. Zhang, B.H. Lu, H.L. Ni, Solvothermal synthesis and thermoelectric properties of lanthanum contained Bi–Te and Bi-Se-Te alloys, Mater. Lett. 59 (2005) 682–685, https://doi.org/10.1016/j.matlet.2004.11.008.

[43] F. Wu, H.Z. Song, J.F. Jia, F. Gao, Y.J. Zhang, X. Hu, Thermoelectric properties of Ce-doped *n*-type $Ce x Bi_{2-}$ $x Te_{2.7}Se_{0.3}$ nanocomposites, Phys. State Solid A 210 (2013) 1183–1189, https://doi.org/10.1002/pssa.201228589.

[44] O. Ivanov, O. Maradudina, R. Lyubushkin, Grain size effect on electrical resistivity of bulk nanograined Bi_2Te_3 material, Mater. Charact. 99 (2015) 175–179, https://doi.org/10.1016/j.matchar.2014.12.0011044-5803.

[45] W. Kim, Strategies for engineering phonon transport in thermoelectrics, J. Mater. Chem. C 3 (2015) 0336–10348, https://doi.org/10.1039/C5TC01670C.

[46] J.S. Blakemore, Solid State Physics, Cambridge University Press, Cambridge, 1985.

[47] H. Kim, Z. Gibbs, Y. Tang, H. Wang, G. Snyder, Characterization of Lorenz number with Seebeck coefficient measurement, APL Mater. 3 (2015), 041506-1-5, https://doi.org/10.1063/1.4908244.